ROYAL SOCIETY OF CHEMISTRY

Check for updates

Comprehensive modelling study of singlet exciton diffusion in donor–acceptor dyads: when small changes in chemical structure matter†

Giacomo Londi, [ID] [a] Rishat Dilmurat,[a] Gabriele D'Avino, [ID] [b] Vincent Lemaur, [ID] [a] Yoann Olivier [ID] [c] and David Beljonne [ID] *[a]

We compare two small π-conjugated donor–bridge–acceptor organic molecules differing mainly in the number of thiophene rings in their bridging motifs (1 ring in **1**; 2 rings in **2**) with the aim of rationalizing the origin of the enhancement in the singlet exciton diffusion coefficient and length of **1** with respect to **2**. By combining force field molecular dynamics and micro electrostatic schemes with time-dependent density functional theory and kinetic Monte Carlo simulations, we dissect the nature of the lowest electronic excitations in amorphous thin films of these molecules and model the transport of singlet excitons across their broadly disordered energy landscapes. In addition to a longer excited-state lifetime associated with a more pronounced intramolecular charge-transfer character, our calculations reveal that singlet excitons in **1** are capable of funneling through long-distance hopping percolation pathways, presumably as a result of the less anisotropic shape of the molecule, which favours long-range 3D transport.

1 Introduction

Bulk heterojunction (BHJ) organic solar cells (OSCs) based on small molecules appear as compelling alternatives to polymer-based OSCs thanks to their peculiar benefits, including high purity, low molecular weight, well-defined and tunable structure, ease of synthesis and processability.[1] So far, the most efficient OSCs based on blends of conjugated-polymer donors and non-fullerene acceptors (NFAs) have reached power conversion efficiencies (PCEs) of over 16% in single-junction devices[2,3] and 17% in tandem cells.[4] These tremendous breakthroughs stem from molecular and device engineering towards reducing or minimizing the losses that affect dramatically the performance of an OSC. Small modifications in the primary chemical structure of the electro-active molecules can turn into large changes in their photo-physical behavior and the resulting optoelectronic response at the device dimensions. We report such an example here, where the focus is on the nature and dynamics of singlet excitations in two small π-conjugated organic molecules:

a {4-[5-(2-phenyl-1,1-dicyanoeth-1-en-2-yl)-2-thienyl]phenyl}diphenyl-amine (TPA-T-DCV-Ph) compound and a 2-(1-{5′-[4-(diphenyl-amino)phenyl]-2,2′-bithien-5-yl}ethylidene)malononitrile (TPA-2T-DCV-Me) one, referred to as **1** and **2**, respectively, in Fig. 1.

These π-conjugated molecules belong to the class of push–pull systems, which in the last decades have found applications as active layers in organic devices, such as dye-sensitized solar cells (DSSC),[5] field-effect transistors (OFET),[6] light-emitting diodes (OLED)[7] and photovoltaic (OPV)[8] cells. Such molecules were designed with the purpose of introducing a partial intra-molecular charge transfer (ICT) character into the lowest exciton states. As these excitons likely feature reduced Coulomb binding energy associated with larger electron–hole separation, they should also be more prompt to dissociate into separated charges at the interface with fullerene electron acceptors. The two D–π–A molecules both comprise a triphenylamine (TPA) fragment, acting as an electron donor (D), and a dicyanovinylene (DCV) moiety, acting as an electron acceptor (A), linked through
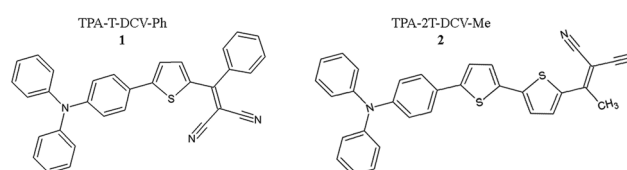
[a] Laboratory for Chemistry of Novel Materials, University of Mons, Place du Parc, 20, 7000 Mons, Belgium. E-mail: David.BELJONNE@umons.ac.be

[b] Institut Néel, CNRS and Grenoble Alpes University, 38042, Grenoble, France

[c] Unité de Chimie Physique Théorique et Structurale & Laboratoire de Physique du solid, Namur Institute of Structured Matter, Université de Namur, Rue de Bruxelles, 61, 5000 Namur, Belgium

† Electronic supplementary information (ESI) available. See DOI: 10.1039/c9cp05201a

Fig. 1 Chemical structures of **1** (left) and **2** (right).

This journal is © the Owner Societies 2019

Phys. Chem. Chem. Phys., 2019, **21**, 25023–25034 | 25023

either a thiophene (in **1**) or a bithiophene (in **2**) π-linker. The electronic excited states in these molecules can be pictured as resulting from the mixing between Frenkel excitations (FE) on the π-conjugated spacer and through-bridge intramolecular D–A charge-transfer (CT) ones. While mixing of CT configurations would red-shift the excitation energies, overlapping electron–hole configurations predominantly feed the oscillator strength, hence enabling large absorption cross-sections in the visible and efficient solar light harvesting. The synthesis of the two dyes and their electrochemical and time-resolved photoluminescence (PL) characterization along with OSC device fabrication and testing have been reported elsewhere.[9–11]

Because it features a more extended conjugated backbone, one would anticipate that **2** has significantly red-shifted optical absorption yielding better overlap with the solar emission spectrum and should thus outperform **1** when used as a donor in BHJ solar cells. It turns out, however, that this is not the case, with significantly larger PCE values reported for **1** ($>5\%$) compared to **2** ($\sim 2\%$) in vacuum-evaporated single solar cells using fullerenes as acceptors. Changes in morphology can be ruled out, as the same trend is observed irrespective of whether the active layer is solution-processed or vacuum-processed. Instead, it was suggested in ref. 11 that this improvement at least partly arises from more efficient singlet exciton diffusion in amorphous films of **1**. As a matter of fact, the reported exciton diffusion length, that is, the distance covered by the singlet excitons during their lifetime, was measured using PL quenching experiments to be significantly larger in **1** (~ 26 nm) compared to **2** (~ 10 nm). This result was attributed to the concerted effects of the longer exciton lifetime, ~ 1.6 ns in **1** *versus* less than 1 ns in **2**, together with the reduced energetic disorder in the smaller molecule. We note that typical values for singlet exciton diffusion lengths in organic semiconductors span the range 5–20 nm and are often limited by static conformational and/or electrostatic disorder.[12,13]

Here, to gain an in-depth microscopic picture of the relationships between primary chemical structure and excited-state properties, we performed a fully atomistic modelling study of the energetics and dynamics of singlet electronic excitations in solid films of **1** and **2**. More specifically, we employed classical molecular dynamics (MD) to simulate the large scale morphologies of the two donors, in order to sample the conformational space in the amorphous (and crystalline) state. The MD morphologies were then employed in time-dependent density functional theory (TD-DFT) and classical Micro Electrostatic (ME) calculations, which allowed the assessment of the nature of the relevant electronic excitations and their energy landscape, fully accounting for environmental effects in the solid state. The results of this combined MD/TD-DFT/ME approach, together with excitonic intermolecular couplings, were then used in kinetic Monte Carlo (KMC) simulations of singlet exciton diffusion, based on the semi-classical Marcus–Levich–Jortner (MLJ) energy transfer rates. Our results confirm the experimental finding that **1** has both a larger exciton diffusion constant and diffusion length with respect to **2**, a feature that arises from the combined effect of the extended lifetime and

the higher likelihood of long-range percolation pathways in the less anisotropic molecule **1**, promoting 3D transport.

2 Theoretical methodology

2.1 Force-field molecular dynamics simulations

In order to model the morphology of these materials, classical force field (FF) MD simulations were carried out. The employed FF was derived from Dreiding,[14] while re-parameterizing the soft inter-ring torsional potentials (see the ESI,† Fig. S1 and S2) against reference MP2/cc-pVDZ calculations, as required for an accurate description of the conformational degrees of freedom. Amorphous phases of the two compounds (from now on **1a** and **2a**) were built using the amorphous builder tool of the Materials Studio (MS) 6.0 package, which implements periodic boundary conditions. The protocol consisted of the following steps: (1) creation of an initial configuration of 1000 molecules in a large 3D periodic cubic box (initial density ~ 0.2 g cm^{-3}); (2) a MD run in the canonical (*NVT*) ensemble at 1000 K for 200 ps to randomize molecular orientations; (3) a MD run in the isothermal–isobaric (*NPT*) ensemble at 1000 K for 1 ns, compressing the sample by progressively increasing the pressure from 1 atm to 1 GPa; (4) a *NPT*-MD run at 1 GPa for 600 ps, gradually cooling down the system from 1000 to 298 K; (5) a *NPT*-MD run at 298 K for 800 ps, releasing the pressure from 1 GPa to 1 atm; and finally (6) a *NPT*-MD run for 2.5 ns at 298 K and 1 atm. In addition, for **1**, a crystalline $8 \times 6 \times 5$ triclinic supercell (from now on **1x**) was generated based on the experimentally resolved crystallographic unit cell,[15] in order to reach a comparable size in terms of the numbers of molecules within the simulation box (960 molecules for **1x** and 1000 molecules for **1a**). The crystalline supercell was subjected to the following steps: (1) a *NVT*-MD run for 200 ps at 298 K; and (2) a *NPT*-MD run for 2.5 ns at 298 K and 1 atm. For both the amorphous and crystalline *NPT*-MD final runs of 2.5 ns, 500 ps was needed for equilibration and 2 ns for production, saving snapshots every 5 ps along the trajectory. The Nosé–Hoover thermostat and the Berendsen barostat (for *NPT* runs) were adopted. The electrostatic interactions were taken into account by calculating the electrostatic potential (ESP) derived atomic charges on the isolated molecule at the MP2 level. MP2 calculations were performed with the GAUSSIAN09[16] suite, while MS 6.0 was adopted for the FF MD simulations.

The reparameterized FF was first benchmarked against experimental data by running simulations on **1x**. Our *NPT*-MD simulations at standard conditions yield a density of $d_{\mathrm{MD}} = 1.23$ g cm^{-3}, in perfect agreement with the experimental value of $d_{\mathrm{exp}} = 1.24$ g cm^{-3}. Also, the predicted cell parameters compare very favorably with the measured crystallographic data, with a relative error of less than 2% (see Table T1 in the ESI†). The densities of the amorphous samples were $d_{\mathrm{MD}} = 1.02$ g cm^{-3} for **1a** (lower than for the crystal, as expected) and $d_{\mathrm{MD}} = 0.97$ g cm^{-3} for **2a**. Moreover, the orientational order in the amorphous samples was assessed by computing the second-rank order parameter $P_2 = \left\langle \dfrac{3\cos^2\theta - 1}{2} \right\rangle$, where θ is the angle

25024 | *Phys. Chem. Chem. Phys.,* 2019, **21**, 25023–25034

This journal is © the Owner Societies 2019

between the long molecular axis and a given reference axis and angular brackets denote the average over the production MD trajectory. We obtained $P_2 = -0.001$ for **1a** and $P_2 = 0.009$ for **2a**, testifying to the isotropic nature of the amorphous samples.

2.2 Excited-state energetics

Electronic structure calculations were performed to track the excited-state energetics for molecular snapshots extracted along the MD trajectories. In the DFT framework, global-hybrid functionals, such as the popular B3LYP[17] and PBE0,[18] are well-known to present shortcomings for the description of CT states in π-conjugated molecules. In addition to the self-interaction error (SIE) and the delocalization one,[19,20] they suffer from a lack of the correct asymptotic behavior in the exchange–correlation energy functional. The latter is recovered in range-separated hybrid (RSH) functionals[21] as adopted in the present study. Specifically, the optimally-tuned (OT) RSH functional ωB97X-D[22,23] was employed. Moreover, according to the "gap tuning" procedure,[24,25] the ω value was finely adjusted in order to match, within 50 meV of tolerance, the HOMO energy with the molecular vertical ionization potential (IP) and the LUMO energy with the vertical electron affinity (EA) of the molecule. Optimized ω values in RSH functionals are usually strongly system-dependent, in particular for π-conjugated molecules, yet they turn out to have very similar values here for **1** ($\omega = 0.139$ Bohr^{-1}) and **2** ($\omega = 0.141$ Bohr^{-1}). These values were kept fixed throughout the DFT and TD-DFT simulations, carried out using GAUSSIAN09[16] with the 6-31G(d,p) basis set, except where otherwise specified.

The effect of the polarizable molecular environment on the intra-molecular excitation energies was accounted for by means of classical ME calculations,[26,27] following our previous work.[28] In a nutshell, ME allows the calculation of a perturbative correction ($\varDelta$, the exciton polarization energy) to the gas-phase TD-DFT lowest energy excitation (S_1), which can be decomposed into an electrostatic and an induction contribution:

$$\varDelta = \varDelta_E + \varDelta_I \qquad (1)$$

where $\varDelta_E$, the electrostatic component, accounts for the interaction of the exciton and the charge densities of the surrounding ground-state molecules, and the induction term $\varDelta_I$ describes the interaction between the excitation and the microscopic dipoles induced in the medium. Self-consistent ME calculations were performed for spherical clusters of 4 nm radius centred around the molecule of interest. The ME model was parametrized with gas-phase ESP[29] atomic charges calculated at the DFT and TD-DFT ωB97X-D/6-311++G(d,p) level for the ground (S_0) and the excited (S_1) state, respectively. The polarizability tensor of the ground-state molecule, computed at the same level of theory mentioned above, was adopted to describe both S_0 and S_1.

TD-DFT calculations were repeated for all individual molecules extracted from the last MD frame and also for 20 molecules (extracted from 400 snapshots) followed along the 2 ns trajectory, thus allowing us to build some statistics in space and time. The fluctuations of the S_1 excitation energy can be quantified by the standard deviation σ_{total} of its distribution. These fluctuations can

be split into two distinct contributions, according to the relevant timescales of the fluctuations: a static contribution (*i.e.* presenting negligible variations over the timescales characterizing exciton lifetimes, ~ 1 ns), which results from the different environment experienced by each molecule, and a dynamic contribution, associated with faster molecular motions:

$$\sigma_{\text{total}} = \sqrt{\sigma_{\text{static}}{}^2 + \sigma_{\text{dynamic}}{}^2} \qquad (2)$$

σ_{total} is obtained as the full S_1 standard deviation for all molecules extracted from the last MD frame. In order to assess the dynamic contribution, 20 molecules were randomly selected and their excitation energies tracked along the 2 ns MD trajectory. The fluctuations around their individual mean lead to the dynamical variance:

$$\sigma_{\text{dynamic}}{}^2 = \frac{1}{n} \sum_{i,k} \left(E_{ik} - \overline{E_k} \right)^2 \qquad (3)$$

where E_{ik} is the S_1 energy of molecule k at time i, $\overline{E_k}$ is the mean energy of molecule k, and n is the number of samples. σ_{static} is then obtained by subtraction from eqn (2).

2.3 Singlet exciton hopping rates and diffusion

Singlet exciton diffusion in the amorphous phase of the two materials was reproduced using a hopping transport model, which is fully justified owing to the much smaller excitonic couplings (< 100 meV) compared to the total relaxation energies (~ 500 meV). The hopping rate was computed using the non-adiabatic semi-classical MLJ expression, which accounts for quantum tunneling effects:[30]

$$\kappa_{\text{if}} = \frac{2\pi}{\hbar} V_{\text{if}}{}^2 \sqrt{\frac{1}{4\pi\lambda_s k_B T}}$$
$$\times \sum_n \left\{ \exp(-S_{\text{eff}}) \frac{S_{\text{eff}}^n}{n!} \times \exp\left[-\frac{\left(\varDelta G_{\text{if}}^0 + \lambda_s + n\hbar\omega_{\text{eff}} \right)^2}{4\lambda_s k_B T} \right] \right\} \qquad (4)$$

where κ_{if} is the exciton hopping rate between molecular sites i and f; V_{if} is the corresponding excitonic coupling; λ_s is the external reorganization energy; k_B is the Boltzmann constant; T is the temperature; $\varDelta G_{\text{if}}^0$ is the Gibbs free energy difference involved in the hopping mechanism; $\hbar\omega_{\text{eff}}$ is the energy of an effective high-frequency intramolecular vibrational mode (the overarching carbon–carbon stretching) that assists the exciton hopping; and $S = \lambda_i/(\hbar\omega_{\text{eff}})$ is the Huang–Rhys factor, which measures the internal reorganization energy λ_i.

Our atomistic calculations were used to provide reliable parameters for eqn (4). Site energies were drawn from a Gaussian distribution with standard deviation σ_{static} and then used to compute inter-site free energy differences $\varDelta G_{\text{if}}^0$. The dynamic disorder σ_{dynamic} is instead related to the total reorganization energy, and specifically for linear exciton–phonon

coupling to a bath of classical harmonic modes:

$$\lambda_{\text{total}} = \frac{\sigma_{\text{dynamic}}^2}{k_B T} \quad (5)$$

In turn, λ_{total} comprises two different contributions:

$$\lambda_{\text{total}} = \lambda_i + \lambda_s \quad (6)$$

where the internal part, λ_i, arises from the difference in the equilibrium geometries between the molecule ground state (S_0) and the first excited state (S_1), while the external part, λ_s, is due to the structural relaxation of the surrounding medium upon energy transfer. Since high-frequency modes are quantum in nature, λ_i can be more safely estimated with the 4-point approach based on DFT/TD-DFT calculations in the gas-phase, namely:

$$\lambda_i = E(S_1|r_0) - E(S_1|r_1) + E(S_0|r_1) - E(S_0|r_0) \quad (7)$$

where $E(S_m|r_n)$ indicates the energy of state S_m at the geometry optimized for state S_n. We note that the geometry optimization in the excited state was performed starting from the ground state geometry and freezing the soft torsional angles, in order to account only for the contribution from the high-frequency modes (and thus avoid double-counting, since the low-frequency modes enter λ_i through the classical MD simulations). The external contribution was then calculated by subtraction from the total reorganization energy, according to eqn (5) and (6).

The excitonic couplings, V_{if}, between molecules in the amorphous samples were computed at the TD-DFT level, resorting to the fragment excitation difference (FED) scheme.[31] The molecular pairs (dimers) were selected according to geometrical criteria: electronic couplings were computed for dimers with a less than 20 Å distance between their center of mass and whose atom–atom distance was found to be smaller than 6 Å. The FED scheme is a diabatization procedure that relies on the calculation of the attachment density (the density of the electron promoted in the transition) and the detachment density (the hole density created in the transition).[32] The electronic couplings are obtained through a unitary transformation that yields the localized diabatic states by maximizing the excitation density difference between the two molecules involved in the energy transfer process. While exchange and overlap might contribute at short intermolecular distances, the Coulomb term is expected to dominate at long range, where it is expected to decay following the usual Förster-like R^{-3} dipole–dipole interaction.

Finally, KMC simulations employing the first reaction method (FRM) algorithm[33] were performed to assess the exciton diffusion coefficient and length. Such a stochastic approach involves the following steps: (1) initialization of the system at time $t = 0$; (2) calculation of the hopping rates from the MLJ equation; (3) quantifying the time for hopping events between an initial (i) and a final site (f) using the following equation:

$$\Delta t_{if} = -\frac{\ln(r)}{\kappa_{if}} \quad (8)$$

where r is a random number generated between 0 and 1 and κ_{if} is the MLJ hopping rate; (4) selecting the event with the smallest t_{if} for the exciton to hop and update its position; and (5) updating the time $t = t + t_{if}$ if t is less than the simulation time (10 ns), or else stopping the simulation. In order to obtain statistically relevant results, and because of the sizeable energetic disorder, a large number of simulations were required (i.e. one million). From the time-dependent mean-square displacements, the averaged singlet exciton diffusion coefficient and diffusion length, L_d, are related through:

$$L_d = \sqrt{D\tau_1} \quad (9)$$

with τ_1 the exciton lifetime.

3 Results and discussion

3.1 Excited-state electronic structure

The ground-state equilibrium geometry of the two molecules was optimized at the ωB97X-D/6-31G(d,p) level of theory. To get insight into the nature of the lowest electronic excitations in the two molecules, we first performed gas-phase TD-DFT calculations at the ground-state geometries. Multiple metrics allow assessing the character of electronic excitations.[34,35] Here, we have opted for the overlap, Φ_s, between the hole and electron densities shown in Fig. 2 for the two molecules. Pure CT excitations correspond to non-overlapping hole and electron density ($\Phi_s = 0$), while fully FE excitations instead lead to $\Phi_s = 1$. The CT or FE character of the excitation depends strictly on the molecular geometry and its fluctuation around equilibrium, as well as on the choice of the exchange–correlation functional.

TD-DFT calculations in the gas phase were also performed to assess the vertical excitation energies. The S_0–S_1 transition energy is 3.15 eV in **1** (with an oscillator strength of 1.167), and 3.04 eV in **2** (with an oscillator strength of 1.657). The excitation energies obtained for single molecules are close to the mean values obtained by sampling the gas-phase conformations using MD simulations in Fig. 5 (see below). The hole and electron density plots in Fig. 2 show that S_1 has a mixed π–π*/CT character,[36] with both the hole and electron density spreading over most of the π-system in both compounds. This translates into Φ_s values of $\sim$0.66 in **1** and $\sim$0.72 in **2**. Thus, extending the bridge from one to two thiophene rings slightly reduces the CT character of the electronic excitations. We next repeated the TD-DFT calculations on all molecules individually extracted from the last MD frame of the three investigated samples (the amorphous **1a** and **2a** and the crystalline **1x**). The results, reported in Fig. 3, show a broad distribution of the hole–electron overlap factors around the values predicted at the equilibrium geometries, clearly associated with thermal fluctuations in the conformation of the molecules. In particular, rotations around the single bonds connecting the donor to the bridge and the bridge to the acceptor (see Fig. S3 in the ESI†) modulate the coupling between the donor and the acceptor groups of the molecule and, therefore, the amount of CT–FE mixing. It is interesting to point out that the Φ_s distributions of
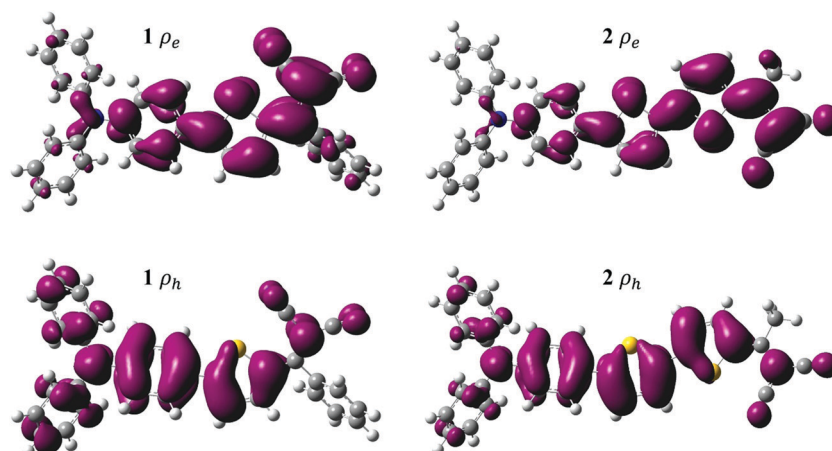
25026 | *Phys. Chem. Chem. Phys.*, 2019, **21**, 25023–25034

This journal is © the Owner Societies 2019

Fig. 2   Hole (ρ_h) and electron (ρ_e) densities calculated in the attachment/detachment formalism for S_1 in **1** (left) and **2** (right), as obtained at the OT–RSH TD-DFT level (ωB97X-D/6-31G(d,p)) based on gas-phase equilibrium ground-state geometries. Isodensity plots were taken at 0.004.
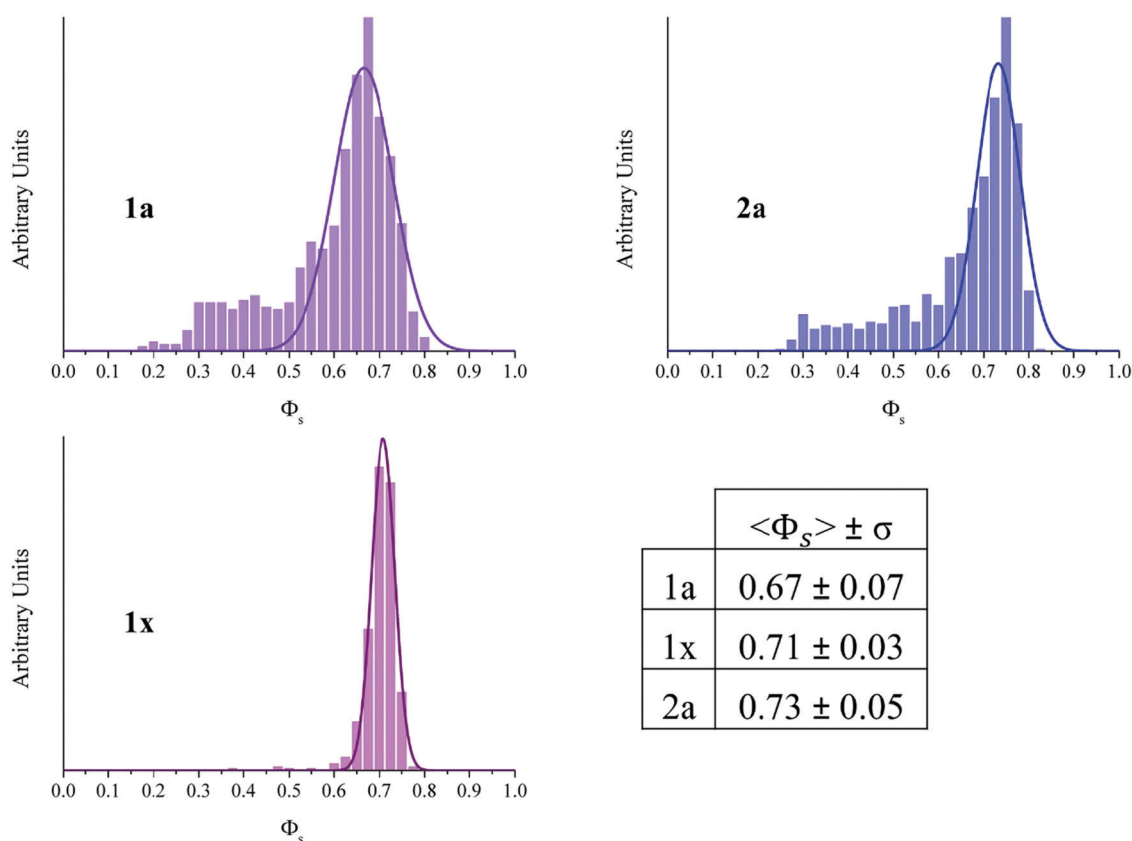

	$\langle \Phi_S \rangle \pm \sigma$
1a	0.67 ± 0.07
1x	0.71 ± 0.03
2a	0.73 ± 0.05

Fig. 3   Room-temperature MD distributions of hole-electron density overlaps Φ_s in S_1 for **1a**, **1x** and **2a**. The averaged Φ_s values and their standard deviations are also reported in the table. Solid lines are Gaussian fits.

the wavefunction overlap are asymmetric, showing a long tail at low Φ_s values that correspond to low-energy conformations, hence possibly slowing down exciton diffusion. As expected, the molecules in the long-range ordered **1x** explore a much smaller region of the conformational space, hence the narrower Φ_s distribution. Very interestingly, Fig. 4 demonstrates that the S_1 excitation energy and its CT character are correlated, with larger CT mixing (lower Φ_s) translating into red-shifted excitations.

This is particularly pronounced for molecule **1**, where conformations yielding the lowest excitation energies are predominantly CT-like, with Φ_s approaching 0.3.

From sampling of the configurational space at room-temperature, exciton Density of States (DOS) distributions were calculated for single molecules either in the gas phase or with fully atomistic electrostatic embedding. The results, portrayed in Fig. 5, show a broad, Gaussian-like, DOS primarily governed
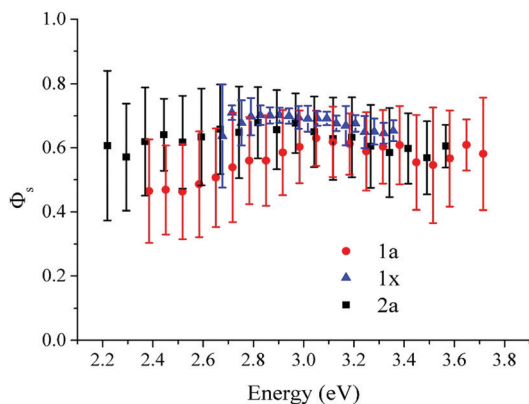
This journal is © the Owner Societies 2019

Phys. Chem. Chem. Phys., 2019, **21**, 25023–25034 | **25027**

Fig. 4 Hole−electron density overlap Φ_s versus transition energy to S_1, as obtained at the OT-RSH TD-DFT level on MD geometries for **1a** (red dots), **1x** (blue triangles) and **2a** (black squares). The data set standard deviation at RT is represented by vertical bars. In the low-energy regime (below ∼3 eV) the correlation coefficient for **1a** is R^2 = 0.95, while for **2a** it is R^2 = 0.76.

by changes in molecular conformation, with different standard deviations obtained in the absence *versus* in the presence of the polarizable environment ($\Delta\sigma_{total}$ < 30 meV). The environmental effects primarily contribute a shift of the distributions, by 0.17 eV for **1a**, 0.13 eV for **1x** and 0.10 eV for **2a**. These small energy corrections reflect the reduced ionic character of the lowest electronic excitations – for the sake of comparison, excess positive or negative charges are typically stabilized by

about 1 eV energy corrections in polarizable molecular crystals.[26,37,38] The most striking feature from Fig. 5 is the rather similar mean values predicted in the amorphous phase of the two molecules, despite the more extended π-bridge in **2** compared to **1**. This is ascribed to the increased CT character in the shorter molecule, as documented above, which compensates for its reduced conjugation length.

We stress that these predictions both qualitatively and quantitatively match with thin-film optical absorption measurements reported in ref. 10 and 11 and in Fig. 5. There, the transition energies measured at λ_{max} for the two molecules almost coincide and the spectral lineshapes can be reasonably fitted with Gaussian functions of standard deviations close to those predicted by theory, although a quantitative comparison with experiment is hampered by the lack of quantum nuclear effects (*i.e.* Franck–Condon structure) and by the assumption of excitons strictly localized on molecular units in the calculations. Moreover, it should be stressed that these large σ values refer to the total width, which encompasses static and dynamic disorder, see Table 1 below. As a side note, we remark that, besides its obvious narrower character, the centre of the energy distribution predicted in crystalline **1** is almost iso-energetic with that in the corresponding amorphous phase. While this might sound surprising at first glance, this is once again the result of the interplay of the molecular conformation (on average more planar in the crystalline phase) and CT–FE mixing (reduced CT character in the crystal). We believe this is a potentially important result,

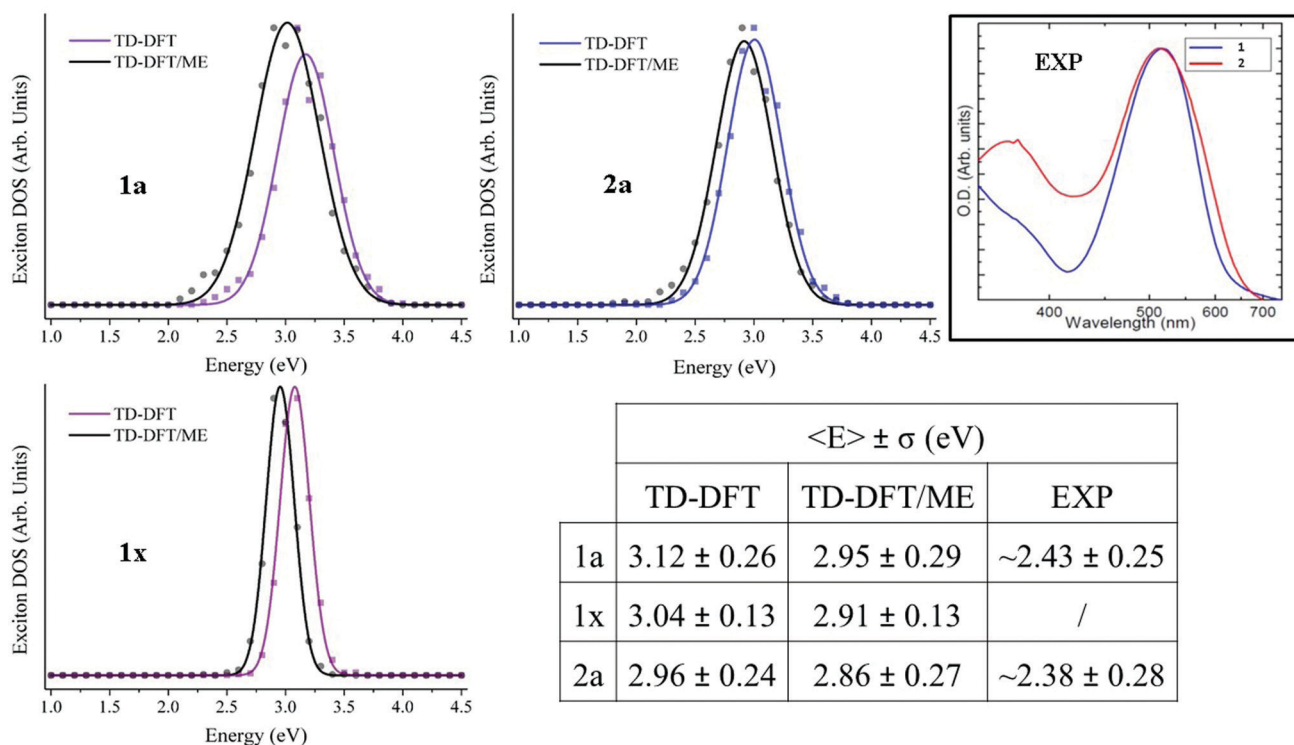|	<E> ± σ (eV)		
	TD-DFT	TD-DFT/ME	EXP
1a	3.12 ± 0.26	2.95 ± 0.29	~2.43 ± 0.25
1x	3.04 ± 0.13	2.91 ± 0.13	/
2a	2.96 ± 0.24	2.86 ± 0.27	~2.38 ± 0.28

Fig. 5 Exciton Density of States (DOS) for the lowest electronic excitation based on gas-phase TD-DFT calculations (coloured) and accounting for electrostatic embedding TD-DFT/ME (in black). Averaged excitation energies and their standard deviations are also reported in the table. Solid lines are Gaussian fits. In the inset, the measured absorption spectra of neat films of **1** and **2** taken from ref. 10 and 11 are shown; their extracted excitation energies and Full Width Half Maximum values are reported also in the table.

25028 | *Phys. Chem. Chem. Phys.*, 2019, **21**, 25023–25034

This journal is © the Owner Societies 2019

Table 1 Calculated σ_{total}, σ_{static} and $\sigma_{dynamic}$ values, along with λ_{total}, λ_i and λ_s ones. σ_{EXP} values extracted from a Gaussian fit of the experimental absorption spectra are also indicated (from ref. 10 and 11)

	σ_{total} (eV)	σ_{exp} (eV)	σ_{static} (eV)	$\sigma_{dynamic}$ (eV)	λ_{total} (eV)	λ_i (eV)	λ_s (eV)
1a	0.294	0.25	0.270	0.115	0.514	0.245	0.269
2a	0.268	0.28	0.243	0.113	0.494	0.296	0.198

as local crystalline domains embedded in an otherwise amorphous matrix usually act as trapping sites. This would not be the case for exciton transport in **1**, which thus should be more resilient to positional disorder and morphological inhomogeneities.

Another molecular characteristic that, in addition to being relevant for the excited-state lifetime and therefore the singlet exciton diffusion length, directly probes the nature of the electronic excited states is the radiative decay rate Γ_{rad}. This quantity may be related to the nature of the excited states in the two compounds, since a larger CT character would result in a smaller transition dipole moment and, hence, a smaller Γ_{rad}. From a perturbative treatment of light–matter interactions, the spontaneous emission rate Γ_{rad} is written as:[39]

$$\Gamma_{rad} = n \frac{\omega_{eg}^3 |\vec{\mu}_{eg}^2|}{3\pi\varepsilon_0\hbar c^3} \qquad (10)$$

where ω_{eg} is the transition frequency from the excited to the ground state, $\vec{\mu}_{eg}$ the transition dipole moment, ε_0 the dielectric vacuum permittivity, $\hbar$ the reduced Planck constant, c the speed of light, and $n = \sqrt{\varepsilon_r}$ the refractive index of the medium, here set equal to 1.49 for a poly(methyl) acrylate (PMMA) matrix (for comparison to the experiments reported in ref. 11). For the three investigated samples, the calculated radiative exciton lifetime, τ_{rad}, averaged over all accessible conformations as explored by room-temperature MD simulations, amounts to 2.6 ns in **1a**, 1.5 ns in **1x** and 1.9 ns in **2a**. The radiative lifetimes are in line with expectations based on the character of the electronic exited states, with namely a larger value for **1** reflecting an increased CT contribution in the amorphous phase. They are also on par with the total lifetimes measured in amorphous films of the two dyes, 2.6 ns and less than 1 ns in **1** and **2**, respectively.[10,11] PL quantum yield measurements using an integrating sphere yield a value of 46% in a powder of **1**,[15] which, combined with the PL total lifetime, provides an experimental estimate for τ_{rad} of about 3.5 ns, in fair agreement with the theoretical value of 2.6 ns. This comforts us in the robustness of our theoretical methodology to properly reproduce the nature and energetics of singlet optical excitations in the molecular materials at hand. Actually, while we are here averaging over the full, broad, exciton DOS, it is likely that low-energy molecular sites contribute predominantly to the PL signal, after (partial) thermalization of the energy carriers.

3.2 Singlet exciton hopping rates

The excited-state energetics enters the MLJ rates in three different ways: (i) the Gibbs free energy, simply equated to the static energetic disorder; and (ii) the external, classical (low-frequency) and (iii) the internal, quantum (high-frequency)

contributions to the nuclear reorganization energies. All these energies can be obtained from our atomistic simulations, provided some educated guess on time-scale separations. Namely, processes that are slow (fast) compared to hopping events were considered static (dynamic). From now on, we will analyze only the exciton diffusion properties for the amorphous pristine materials in order to provide a better comparison among our investigated samples. The calculated data that feed the MLJ equation for **1a** and **2a** are collected in Table 1.

The energetic disorder is primarily caused by nuclear motions that are slow relative to exciton hopping, and thus static in nature. These likely involve large-amplitude changes in the conformation of the molecules, which are slowed down by packing effects in the solid. Much faster (internal) reorganization in bond lengths mediated by high-frequency stretching/breathing modes and small (external) rearrangement around the intramolecular equilibrium geometry induced by the environment contribute with similar weights to the total reorganization energy.

We now discuss the excitonic couplings, V_{if}, mediating singlet exciton hopping and the MLJ hopping rates, κ_{if}. The FED values are plotted as a function of the intermolecular distance between centers of mass in Fig. 6 top. For comparison, we show in Fig. 6 bottom the corresponding couplings obtained by retaining only Coulomb interactions in the point dipole–point dipole approximation (PDA). As documented previously,[31] this approximation fails at short distances where it produces erroneously large couplings. At long distances, FED and PDA show the expected inverse cubic distance dependence.

A more useful metric for the interactions between molecules is the electronic connectivity or effective coordination number, defined as the number, $n(V_{th})$, of neighbor molecules f coupled to a central molecule i with a coupling V_{if} larger than a given threshold value V_{th}. As expected, $n(V_{th})$ decreases with V_{th} to reach values close to zero for couplings larger than $\sim$40 meV, Fig. 7.
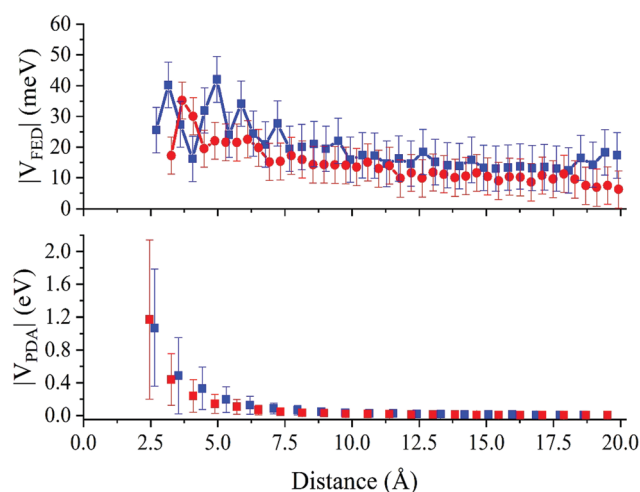

Fig. 6 Excitonic coupling calculated with the FED scheme (top) and in the point dipole–point dipole approximation (bottom) for **1a** (in red) and **2a** (in blue). The data set standard deviation is represented by vertical bars.

This journal is © the Owner Societies 2019

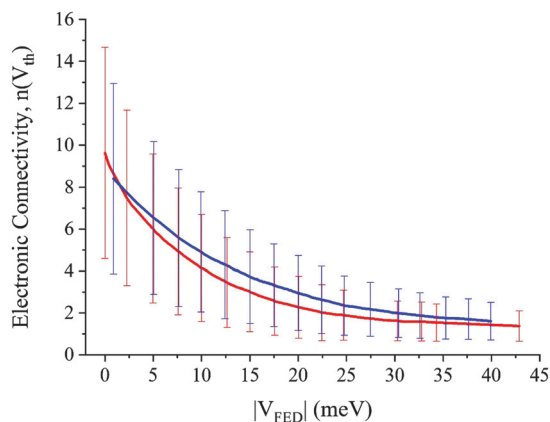*Phys. Chem. Chem. Phys.*, 2019, **21**, 25023–25034 | 25029

Fig. 7 Electronic connectivity calculated with the FED scheme for **1a** (in red) and **2a** (in blue). The data set standard deviation is represented by vertical bars.

Fig. 9 Average exciton energy as a function of the KMC simulation time for **1a** (in red) and **2a** (in blue). The data set standard deviation is represented by vertical bars.

The two molecules show similar evolutions with, on average, 2–6 molecules displaying excitonic couplings in the range 10–25 meV. Combining these excitonic couplings with the internal and external reorganization energies listed in Table 1, we obtained the distributions of nearest neighbor exciton hopping rates, shown in Fig. 8. These span about six orders of magnitude in timescale with a long tail at small κ_{if} corresponding to unlikely events associated with poorly connected molecules. For both molecules, the rate distributions peak at around 0.1–1 ps^{-1}, which is significantly faster than the exciton lifetimes, thus allowing for multiple jumps during the exciton lifespan.

3.3 Singlet exciton diffusion

KMC simulations were performed to model the exciton dynamics. In a first set of simulations, we assumed as initial conditions broad band excitation, that is, all molecular sites were excited with the same probability irrespective of their energy. We start by analysing the time evolution of the average exciton energy. The results, reported in Fig. 9, clearly show two different regimes. At early times after light absorption (<10 ps), there is a rapid

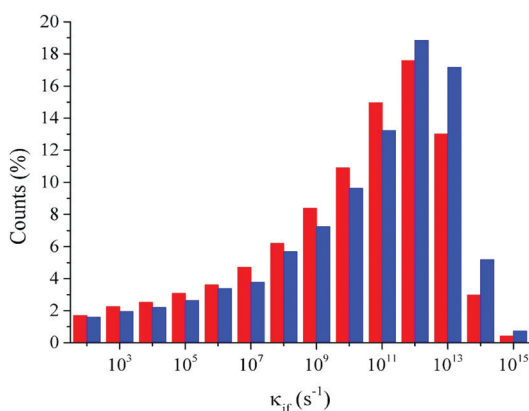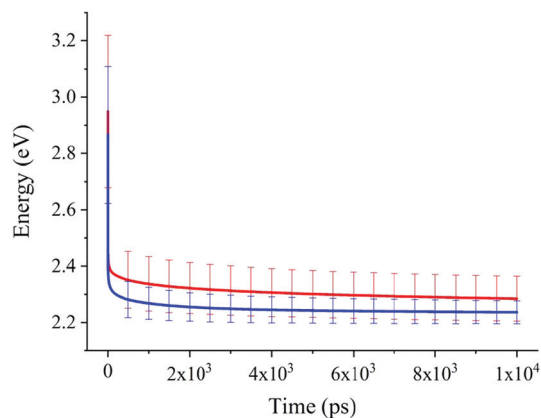Fig. 8 MLJ exciton hopping rate κ_{if} distribution calculated for **1a** (in red) and **2a** (in blue).

and large (about half-an-eV) drop in energy attributed to non-equilibrium relaxation processes from initially hot energy carriers. At longer timescales, the system keeps cooling down at a much slower pace, with no sign of full thermalization during the exciton lifetime. At this point, we can already conclude that exciton diffusion in these disordered molecular materials proceeds largely in a non-equilibrium manner. This is corroborated by the calculated mean square displacement over time ratio in Fig. 10. In the normal diffusion regime, this ratio should converge to a time-independent value at equilibrium conditions, which is not reached during the excited-state lifetime in our simulations. Yet, for the sake of simplicity, we will keep referring to the equilibrium concept of the diffusion coefficient in the following. With this caveat, it is interesting to notice that for simulation times commensurate with the singlet lifetime (1–2 ns) D is slightly larger for **1** compared to **2**, see Fig. 10a and Table 2. We will return to this point later but the consequence of this difference in the diffusion coefficient, together with the longer-lived singlet exciton, is that molecule **1** shows a significantly larger exciton diffusion length than **2**, see Fig. 10b and Table 2 (where we used the measured total lifetimes). In view of the multifaceted aspect and complexity of the modelling approach, the calculated L_d values are in remarkable agreement with experiment, see Table 2.

We discussed before the origin of the difference in exciton lifetimes between the two molecules, namely the various amount of charge-transfer mixing in the lowest electronic excitations. In view of the very similar excitonic coupling and rate distributions shown in Fig. 6 and 8 respectively, it is, however, not obvious why **1** features an improved diffusion coefficient over **2**. We believe this is rooted in the more efficient percolation pathways available for excitons in the shorter molecule, in analogy with the random resistance network for charge transport in organics.[40] To test this idea, we assessed the averaged length covered by excitons that hop between molecular sites within a given range of rates. The corresponding distributions are shown for the two molecules in Fig. 11, considering hopping frequencies for the most likely events (in the range of 10^9–10^{11} s^{-1}).

25030 | *Phys. Chem. Chem. Phys.*, 2019, **21**, 25023–25034

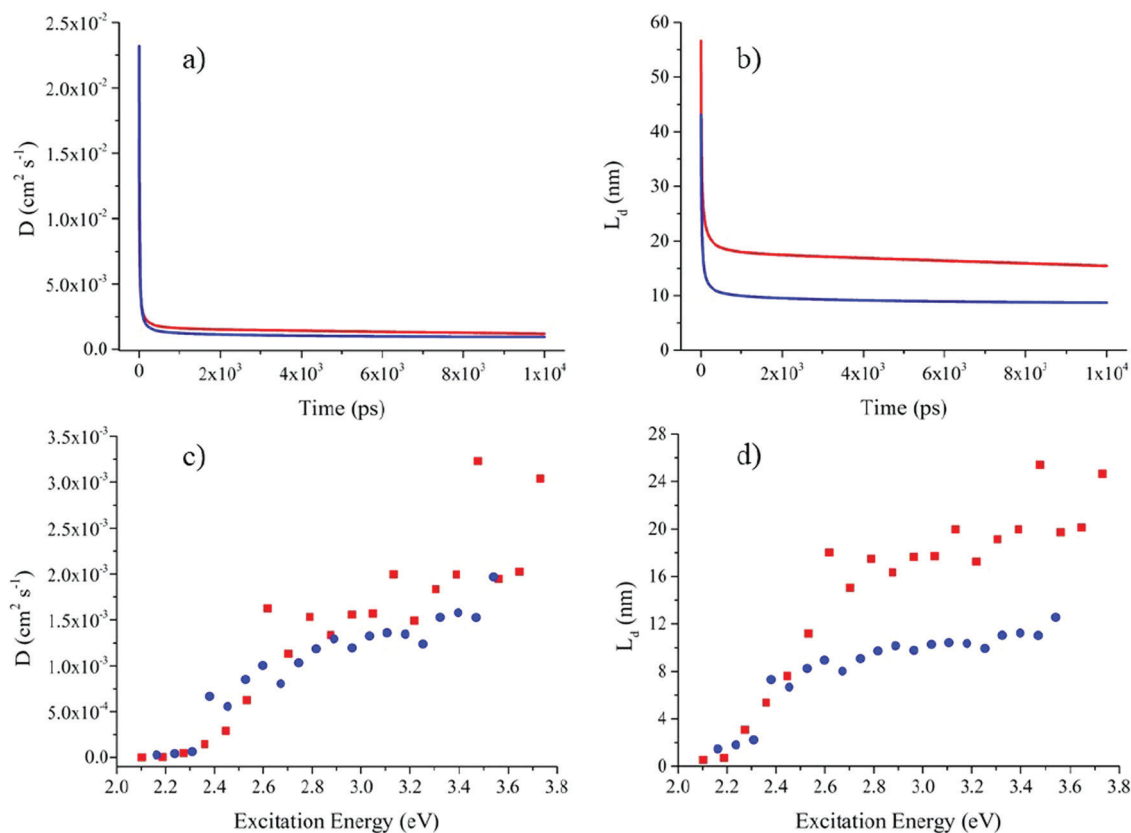This journal is © the Owner Societies 2019

Fig. 10 In the upper panel, the calculated (a) diffusion coefficient, D, and (b) exciton diffusion length, L_d, for **1a** (in red) and **2a** (in blue). In the bottom panel, the same quantities, respectively in (c) and in (d), were calculated using the 'site-selective' excitations method.

Table 2 Calculated diffusion coefficient at the exciton lifetime and exciton diffusion length for **1a** and **2a**. The experimental values[10,11] for the latter are also reported

	Diffusion coefficient ($cm^2 \ s^{-1}$)	Diffusion length (nm)	
		Exp.	Calc.
1a	1.53×10^{-3}	~ 26	18
2a	1.28×10^{-3}	~ 10	10

The distributions are clearly shifted towards longer distances for **1** compared to **2**, rationalizing the difference in diffusion coefficient. Thus, it appears that there are more long-distance continuous hopping pathways that the excitons can funnel through in the smaller compound **1**, presumably as a result of its reduced anisotropic shape favouring 3D transport.

To close this part, we would like to come back to the non-equilibrium nature of singlet exciton transport in these molecular materials. As previously proposed by Bässler and co-workers,[41] a useful set of numerical experiments to probe energetic disorder in organics is to run diffusion simulations using energy-selective excitations, namely generating excitons only on molecular sites matching a given energy window. Consistent with the disorder model, Fig. 10c and d show a strong dependence of the 'effective' diffusion coefficient and length with excitation energy. While high-energy excitons can easily find electronically coupled nearest neighbours with lower energy and thus undergo fast downhill migration, excitons at the bottom of the DOS are instead surrounded by a smaller number of thermally accessible sites and move *via* slow uphill hopping events.

4 Conclusions

We have performed a comprehensive theoretical investigation of the nature and dynamics of electronic excitations in two small π-conjugated organic molecules that differ mostly by one thiophene ring in their bridging unit. Earlier experimental reports point to a somewhat unexpected increase in PCE for **1** with respect to **2** in vacuum-evaporated OSCs using fullerenes as acceptors,[9,10] a result that was explained by the improved singlet exciton diffusion in **1**. It was tentatively concluded that the larger diffusion coefficient and diffusion length in the shorter molecule stem from a longer exciton lifetime and reduced energetic disorder. Our multiscale computation approach, combining MD, TD-DFT and ME calculations with KMC simulations, yields similar overall conclusions, yet for slightly different reasons. The MD/TD-DFT/ME results show that the lowest singlet electronic excitations in these molecules have a mixed localized/charge-transfer nature, which largely fluctuates in time and space as a result of conformational motion. On average **1** displays slightly more pronounced CT character, which explains why it absorbs at about the same

This journal is © the Owner Societies 2019

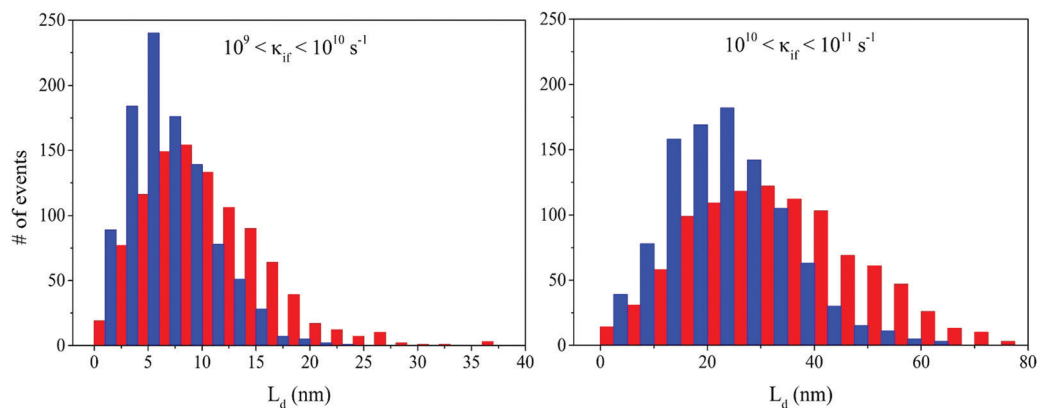*Phys. Chem. Chem. Phys.*, 2019, **21**, 25023–25034 | **25031**

Fig. 11 Percolation pathways calculated in two different ranges of exciton hopping rates for **1a** (in red) and **2a** (in blue).

wavelength as **2**, despite its shorter conjugated backbone. As a consequence of its increased CT character, **1** features a longer (radiative) lifetime compared to **2**, in line with the experimental findings and in part responsible for the extended exciton diffusion lengths. The full spectral linewidths of the excitation energy distributions are very large (>0.2 eV) in both molecules because of both conformation and dielectric disorder in the amorphous films. In such a disordered energy landscape, exciton diffusion proceeds largely in a non-equilibrium regime during the finite excited-state lifetime. Close to equilibrium, the diffusion coefficient predicted from KMC simulations is larger for **1** compared to **2**, although the total energetic disorder computed for the two molecules is comparable. The difference in exciton migration in fact reflects the existence of long-range, efficient percolation pathways, likely arising from the slightly less anisotropic shape of **1** prompting three-dimensional transport. As a concluding remark, it is important to highlight that the amount of energy disorder actually probed by ps transient experiments as performed in ref. 11 is only a fraction of the total disorder, because in addition to the ultrafast energy drop at very early timescales that requires sub-ps resolution, full energy relaxation has not completed during the exciton lifespan. Rather, fs-resolved photoluminescence measurements using site-selective excitations are required to cover the broad dynamic range in energy distribution present in these inherently disordered soft molecular materials. Despite, or perhaps thanks to, their large energetic disorder, molecules such as **1** appear to be very promising candidates for energy photoconversion. We speculate that, in analogy with electron transport in fullerenes and some of the novel non-fullerene acceptors,[42–47] the 3D excitonic conductivity of **1** is key to drive long-range exciton motion at dissociation spots.

Conflicts of interest

There are no conflicts to declare.

Acknowledgements

Notes and references

1 F. Bureš, Fundamental aspects of property tuning in push–pull molecules, *RSC Adv.*, 2014, **4**(102), 58826–58851.

2 J. Yuan, Y. Zhang, L. Zhou, G. Zhang, H.-L. Yip and T.-K. Lau, *et al.*, Single-Junction Organic Solar Cell with over 15% Efficiency Using Fused-Ring Acceptor with Electron-Deficient Core, *Joule*, 2019, **3**(4), 1140–1151.

3 Y. Cui, H. Yao, J. Zhang, T. Zhang, Y. Wang and L. Hong, *et al.*, Over 16% efficiency organic photovoltaic cells enabled by a chlorinated acceptor with increased open-circuit voltages, *Nat. Commun.*, 2019, **10**(1), 2515.

4 L. Meng, Y. Zhang, X. Wan, C. Li, X. Zhang and Y. Wang, *et al.*, Organic and solution-processed tandem solar cells with 17.3% efficiency, *Science*, 2018, **361**(6407), 1094–1098.

5 B. O'Regan and M. Grätzel, A low-cost, high-efficiency solar cell based on dye-sensitized colloidal TiO_2 films, *Nature*, 1991, **353**(6346), 737–740.

6 S. Allard, M. Forster, B. Souharce, H. Thiem and U. Scherf, Organic Semiconductors for Solution-Processable Field-Effect Transistors (OFETs), *Angew. Chem., Int. Ed.*, 2008, **47**(22), 4070–4098.

7 Y. Ohmori, Development of organic light-emitting diodes for electro-optical integrated devices, *Laser Photonics Rev.*, 2010, **4**(2), 300–310.

8 A. W. Hains, Z. Liang, M. A. Woodhouse and B. A. Gregg, Molecular Semiconductors in Organic Photovoltaic Cells, *Chem. Rev.*, 2010, **110**(11), 6689–6735.

9 A. N. Bakiev, D. G. Selivanova, I. V. Lunegov, A. N. Vasyanin, O. A. Maiorova and A. A. Gorbunov, *et al.*, Novel thiophene-containing push-pull chromophores that include carbazole and

25032 | *Phys. Chem. Chem. Phys.*, 2019, **21**, 25023–25034

This journal is © the Owner Societies 2019

triphenylamine moieties: study of optical and electrochemical properties, *Chem. Heterocycl. Compd.*, 2016, **52**(6), 379–387.

10 O. V. Kozlov, X. Liu, Y. N. Luponosov, A. N. Solodukhin, V. Y. Toropynina and J. Min, *et al.*, Triphenylamine-Based Push–Pull Molecule for Photovoltaic Applications: From Synthesis to Ultrafast Device Photophysics, *J. Phys. Chem. C*, 2017, **121**(12), 6424–6435.

11 O. V. Kozlov, Y. N. Luponosov, A. N. Solodukhin, B. Flament, O. Douhéret and P. Viville, *et al.*, Simple donor-acceptor molecule with long exciton diffusion length for organic photovoltaics, *Org. Electron.*, 2018, **53**, 185–190.

12 S. Athanasopoulos, E. V. Emelianova, A. B. Walker and D. Beljonne, Exciton diffusion in energetically disordered organic materials, *Phys. Rev. B: Condens. Matter Mater. Phys.*, 2009, **80**(19), 195209.

13 S. Athanasopoulos, E. Hennebicq, D. Beljonne and A. B. Walker, Trap Limited Exciton Transport in Conjugated Polymers, *J. Phys. Chem. C*, 2008, **112**(30), 11532–11538.

14 S. L. Mayo, B. D. Olafson and W. A. Goddard, Dreiding: a generic force field for molecular simulations, *J. Phys. Chem.*, 1990, **94**(26), 8897–8909.

15 Courtesy of Enikolopov Institute of Synthetic Polymeric Materials of the Russian Academy of Sciences.

16 M. J. Frisch, G. W. Trucks, H. B. Schlegel, G. E. Scuseria, M. A. Robb, J. R. Cheeseman, G. Scalmani, V. Barone, B. Mennucci, G. A. Petersson, H. Nakatsuji, M. Caricato, X. Li, H. P. Hratchian, A. F. Izmaylov, J. Bloino, G. Zheng, J. L. Sonnenberg and M. Had, *Gaussian 09, Revision D.01*, 2009.

17 P. J. Stephens, F. J. Devlin, C. F. Chabalowski and M. J. Frisch, Ab Initio Calculation of Vibrational Absorption and Circular Dichroism Spectra Using Density Functional Force Fields, *J. Phys. Chem.*, 1994, **98**(45), 11623–11627.

18 C. Adamo and V. Barone, Toward reliable density functional methods without adjustable parameters: The PBE0 model, *J. Chem. Phys.*, 1999, **110**(13), 6158–6170.

19 L. Kronik, T. Stein, S. Refaely-Abramson and R. Baer, Excitation Gaps of Finite-Sized Systems from Optimally Tuned Range-Separated Hybrid Functionals, *J. Chem. Theory Comput.*, 2012, **8**(5), 1515–1531.

20 T. Körzdörfer and J.-L. Brédas, Organic Electronic Materials: Recent Advances in the DFT Description of the Ground and Excited States Using Tuned Range-Separated Hybrid Functionals, *Acc. Chem. Res.*, 2014, **47**(11), 3284–3291.

21 T. Yanai, D. P. Tew and N. C. Handy, A new hybrid exchange–correlation functional using the Coulomb-attenuating method (CAM-B3LYP), *Chem. Phys. Lett.*, 2004, **393**(1), 51–57.

22 J.-D. Chai and M. Head-Gordon, Long-range corrected hybrid density functionals with damped atom–atom dispersion corrections, *Phys. Chem. Chem. Phys.*, 2008, **10**(44), 6615–6620.

23 J.-D. Chai and M. Head-Gordon, Systematic optimization of long-range corrected hybrid density functionals, *J. Chem. Phys.*, 2008, **128**(8), 84106.

24 K. Do, M. K. Ravva, T. Wang and J.-L. Brédas, Computational Methodologies for Developing Structure–Morphology–Performance Relationships in Organic Solar Cells: A Protocol Review, *Chem. Mater.*, 2017, **29**(1), 346–354.

25 H. Sun, C. Zhong and J.-L. Brédas, Reliable Prediction with Tuned Range-Separated Functionals of the Singlet–Triplet Gap in Organic Emitters for Thermally Activated Delayed Fluorescence, *J. Chem. Theory Comput.*, 2015, **11**(8), 3851–3858.

26 G. D'Avino, L. Muccioli, C. Zannoni, D. Beljonne and Z. G. Soos, Electronic Polarization in Organic Crystals: A Comparative Study of Induced Dipoles and Intramolecular Charge Redistribution Schemes, *J. Chem. Theory Comput.*, 2014, **10**(11), 4959–4971.

27 G. D'Avino, L. Muccioli, F. Castet, C. Poelking, D. Andrienko and Z. G. Soos, *et al.*, Electrostatic phenomena in organic semiconductors: Fundamentals and implications for photovoltaics, *J. Phys.: Condens. Matter*, 2016, **28**(43), 433002.

28 Y. Olivier, B. Yurash, L. Muccioli, G. D'Avino, O. Mikhnenko and J. C. Sancho-García, *et al.*, Nature of the singlet and triplet excitations mediating thermally activated delayed fluorescence, *Phys. Rev. Mater.*, 2017, **1**(7), 75602.

29 B. H. Besler, K. M. Merz Jr. and P. A. Kollman, Atomic charges derived from semiempirical methods, *J. Comput. Chem.*, 1990, **11**(4), 431–439.

30 J. Jortner, Temperature dependent activation energy for electron transfer between biological molecules, *J. Chem. Phys.*, 1976, **64**(12), 4860–4867.

31 C.-P. Hsu, Z.-Q. You and H.-C. Chen, Characterization of the Short-Range Couplings in Excitation Energy Transfer, *J. Phys. Chem. C*, 2008, **112**(4), 1204–1212.

32 M. Head-Gordon, A. M. Grana, D. Maurice and C. A. White, Analysis of Electronic Transitions as the Difference of Electron Attachment and Detachment Densities, *J. Phys. Chem.*, 1995, **99**(39), 14261–14270.

33 D. T. Gillespie, A general method for numerically simulating the stochastic time evolution of coupled chemical reactions, *J. Comput. Phys.*, 1976, **22**(4), 403–434.

34 Y. Olivier, J.-C. Sancho-Garcia, L. Muccioli, G. D'Avino and D. Beljonne, Computational Design of Thermally Activated Delayed Fluorescence Materials: The Challenges Ahead, *J. Phys. Chem. Lett.*, 2018, **9**(20), 6149–6163.

35 E. W. Evans, Y. Olivier, Y. Puttisong, W. K. Myers, T. J. H. Hele and S. M. Menke, *et al.*, Vibrationally Assisted Intersystem Crossing in Benchmark Thermally Activated Delayed Fluorescence Molecules, *J. Phys. Chem. Lett.*, 2018, **9**(14), 4053–4058.

36 O. V. Kozlov, Y. N. Luponosov, S. A. Ponomarenko, N. Kausch-Busies, D. Y. Paraschuk and Y. Olivier, *et al.*, Ultrafast Charge Generation Pathways in Photovoltaic Blends Based on Novel Star-Shaped Conjugated Molecules, *Adv. Energy Mater.*, 2015, **5**(7), 1401657.

37 F. Castet, G. D'Avino, L. Muccioli, J. Cornil and D. Beljonne, Charge separation energetics at organic heterojunctions: on the role of structural and electrostatic disorder, *Phys. Chem. Chem. Phys.*, 2014, **16**(38), 20279–20290.

38 G. D'Avino, Y. Olivier, L. Muccioli and D. Beljonne, Do charges delocalize over multiple molecules in fullerene derivatives?, *J. Mater. Chem. C*, 2016, **4**(17), 3747–3756.

This journal is © the Owner Societies 2019

Phys. Chem. Chem. Phys., 2019, **21**, 25023–25034 | **25033**

39 R. A. L. Vallée, M. Van Der Auweraer, F. C. De Schryver, D. Beljonne and M. Orrit, A Microscopic Model for the Fluctuations of Local Field and Spontaneous Emission of Single Molecules in Disordered Media, *ChemPhysChem*, 2005, **6**(1), 81–91.

40 H. Sirringhaus, 25th Anniversary Article: Organic Field-Effect Transistors: The Path Beyond Amorphous Silicon, *Adv. Mater.*, 2014, **26**(9), 1319–1335.

41 H. Bässler and B. Schweitzer, Site-Selective Fluorescence Spectroscopy of Conjugated Polymers and Oligomers, *Acc. Chem. Res.*, 1999, **32**(2), 173–182.

42 S. Holliday, R. S. Ashraf, A. Wadsworth, D. Baran, S. A. Yousaf and C. B. Nielsen, *et al.*, High-efficiency and air-stable P3HT-based polymer solar cells with a new non-fullerene acceptor, *Nat. Commun.*, 2016, **7**(1), 11585.

43 J. Liu, S. Chen, D. Qian, B. Gautam, G. Yang and J. Zhao, *et al.*, Fast charge separation in a non-fullerene organic solar cell with a small driving force, *Nat. Energy*, 2016, **1**, 16089.

44 X. Che, Y. Li, Y. Qu and S. R. Forrest, High fabrication yield organic tandem photovoltaics combining vacuum- and solution-processed subcells with 15% efficiency, *Nat. Energy*, 2018, **3**(5), 422–427.

45 P. Cheng, G. Li, X. Zhan and Y. Yang, Next-generation organic photovoltaics based on non-fullerene acceptors, *Nat. Photonics*, 2018, **12**(3), 131–142.

46 J. Zhang, H. S. Tan, X. Guo, A. Facchetti and H. Yan, Material insights and challenges for non-fullerene organic solar cells based on small molecular acceptors, *Nat. Energy*, 2018, **3**(9), 720–731.

47 C. Yan, S. Barlow, Z. Wang, H. Yan, A. K.-Y. Jen and S. R. Marder, *et al.*, Non-fullerene acceptors for organic solar cells, *Nat. Rev. Mater.*, 2018, **3**, 18003.